

## Astrophysics equation of state inference with Bayesian chiral effective field theory uncertainties

MELISSA MENDES <sup>1,2,3</sup> HANNAH GÖTTLING <sup>1,2</sup> ANNA HENSEL <sup>1</sup> ISAK SVENSSON <sup>1,2,3</sup> KAI HEBELER <sup>1,2,3</sup>  
ACHIM SCHWENK <sup>1,2,3</sup> NATHAN RUTHERFORD <sup>4</sup> AND ANNA WATTS <sup>5,6</sup>

<sup>1</sup>*Technische Universität Darmstadt, Department of Physics, 64289 Darmstadt, Germany*

<sup>2</sup>*ExtreMe Matter Institute EMMI, GSI Helmholtzzentrum für Schwerionenforschung GmbH, 64291 Darmstadt, Germany*

<sup>3</sup>*Max-Planck-Institut für Kernphysik, Saupfercheckweg 1, 69117 Heidelberg, Germany*

<sup>4</sup>*Foundational Questions Institute (FQxI), 235 Ponce de Leon PI M 217, Decatur, GA 30030, USA*

<sup>5</sup>*Anton Pannekoek Institute for Astronomy, University of Amsterdam, Science Park 904, 1098 XH Amsterdam, The Netherlands*

<sup>6</sup>*Gravitation and Astroparticle Physics Amsterdam (GRAPPA), University of Amsterdam, 1098 XH Amsterdam, The Netherlands*

### ABSTRACT

We investigate Bayesian chiral effective field theory ( $\chi$ EFT) uncertainties, which assign a statistical interpretation to equation of state (EOS) distributions near nuclear saturation density,  $n_0$ , as well as constraints from perturbative quantum chromodynamics (pQCD) to Bayesian EOS inference from LIGO/Virgo, NICER and pulsar mass observations. The tails of the  $\chi$ EFT uncertainties allow for broader pressure ranges in our priors, but large parts of these are excluded by the astrophysical observations, so that the EOS and the resulting mass-radius posteriors are still very consistent with our earlier work. Within our broad prior ranges, we observe a clear stiffening of the EOS at  $n \gtrsim 3n_0$ . Moreover, the impact of the pQCD constraints on the posterior EOS and mass-radius range is negligible due to the astrophysics constraints. Exploiting the strong correlation between pure neutron matter and matter in beta equilibrium, we infer the symmetry energy slope parameter  $L$  from astrophysics. For the 68% credible interval, we obtain  $L = 42.6 - 52$  MeV and  $L = 44.2 - 56.7$  MeV using piecewise-polytrope and speed-of-sound high-density extensions, respectively. The  $L$  posterior is mainly driven by the combination of GW170817 LIGO/Virgo and PSR J0740+6620, PSR J0437-4715, and PSR J0614-3329 NICER observations.

*Keywords:* dense matter — equation of state — stars: neutron — X-rays: stars — gravitational waves

### 1. INTRODUCTION

Neutron stars are natural laboratories for studying the equation of state (EOS) of dense matter (J. M. Lattimer 2021; K. Chatziioannou et al. 2025). Astrophysical observations of high-mass pulsars (P. Demorest et al. 2010; J. Antoniadis et al. 2013; E. Fonseca et al. 2016; H. T. Cromartie et al. 2020; E. Fonseca et al. 2021) set lower limits on the maximum mass of neutron stars. Combined with tidal deformabilities from LIGO/Virgo gravitational wave measurements (B. P. Abbott et al. 2019, 2020) and NICER mass-radius information (M. C. Miller et al. 2019; T. E. Riley et al. 2019; M. C. Miller et al. 2021; T. E. Riley et al. 2021; T. Salmi et al. 2022, 2023; D. Choudhury et al. 2024; A. J. Dittmann et al. 2024; T. Salmi et al. 2024a,b; S. Vinciguerra et al. 2024; M. Hoogkamer et al. 2025; L. Mauviard et al. 2025; M. Hoogkamer et al. 2026; M. C. Miller et al. 2026; L. Qi

et al. 2025; Y. Kini et al. 2026), this provides strong constraints on the EOS at supranuclear densities.

Going from the astrophysical data to the EOS typically involves the inclusion of nuclear physics constraints through the neutron star crust and the properties of neutron-rich matter around saturation density. This has benefited from advances using chiral effective field theory ( $\chi$ EFT) with powerful many-body calculations to reliably predict the EOS of neutron matter up to around  $1.5n_0$  (with saturation density  $n_0 = 0.16 \text{ fm}^{-3}$ ) (K. Hebeler et al. 2013; I. Tews et al. 2013; J. E. Lynn et al. 2016; C. Drischler et al. 2019; J. Keller et al. 2023; I. Tews et al. 2025; F. Alp et al. 2025; C. Drischler et al. 2026) and matter in beta equilibrium with quantified uncertainties (J. Keller et al. 2023; H. Göttling et al. 2025). Beyond nuclear densities, this is combined with general high-density extensions that are agnostic of the particle composition and interactions, using, for example, piece-

wise polytropes (J. S. Read et al. 2009; K. Hebeler et al. 2013), speed-of-sound parameterizations (I. Tews et al. 2018; S. K. Greif et al. 2019), piecewise speed-of-sound models (L. Brandes et al. 2023; H. Koehn et al. 2025), or Gaussian processes (GPs) (P. Landry et al. 2020; R. Essick et al. 2020; S. Ng et al. 2025; T. Gorda et al. 2026), combined with Bayesian statistical frameworks to infer the EOS of neutron star matter.

In addition, GPs have recently been used to provide Bayesian estimates of the  $\chi$ EFT truncation uncertainties from order-by-order calculations around saturation density (C. Drischler et al. 2020a,b; H. Götting et al. 2025). Moreover, at larger densities, for  $n \gtrsim 40 - 50n_0$ , constraints on the EOS based on perturbative quantum chromodynamics (pQCD) calculations have been derived (T. Gorda et al. 2021a,b; O. Komoltsev & A. Kurkela 2022). Even though these densities are far beyond those reached in neutron stars, it remains an interesting question how pQCD constraints further constrain the EOS within the relevant density regime of neutron stars, as investigated in O. Komoltsev et al. (2024); H. Koehn et al. (2025).

In this context, the goal of this work is to incorporate the new GP-based Bayesian  $\chi$ EFT uncertainties and constraints from pQCD in our neutron star Bayesian EOS inference framework, N<sub>EO</sub>ST (G. Raaijmakers et al. 2025)<sup>1</sup>. In particular, we will study the impact of the Bayesian  $\chi$ EFT uncertainties for matter in beta equilibrium from H. Götting et al. (2025) at  $0.5n_0 \leq n \leq 1.5n_0$ , and implement EOS extensions that are consistent with pQCD at extreme densities, following the procedure described in O. Komoltsev & A. Kurkela (2022). Compared to our previous work (G. Raaijmakers et al. 2020; G. Raaijmakers et al. 2021; N. Rutherford et al. 2024; L. Mauviard et al. 2025), the use of a  $\chi$ EFT distribution allows us to infer the slope parameter  $L$  of the symmetry energy from astrophysical data and to test which observations are most constraining for  $L$ . The  $L$  parameter has been studied from various EOS constructions and inferences (see, for example, R. Essick et al. (2021); B. Hu et al. (2022); R. W. Fearick et al. (2023); J. M. Lattimer (2023)) and it also correlates with observables from nuclear experiment such as the neutron skin thickness.

This paper is organized as follows. In Section 2, we briefly review the Bayesian EOS inference framework used. We discuss the introduction of the Bayesian  $\chi$ EFT uncertainties in Section 3 and the inclusion of pQCD-compatible extensions in Section 4. In Section 5, we

study the impact of these on the EOS and the resulting mass-radius posteriors based on gravitational-wave observations from LIGO/Virgo and pulse-profile modeling from NICER, including the high-mass pulsar information. In particular, we also present results for the inferred symmetry energy slope parameter  $L$ . Finally, we summarize our main findings in Section 6. The code and data needed to reproduce our results will be made publicly available.

## 2. EOS INFERENCE FRAMEWORK

We use the open-source EOS inference code N<sub>EO</sub>ST (G. Raaijmakers et al. 2025), which implements the Bayesian inference framework used in previous studies (S. K. Greif et al. 2019; G. Raaijmakers et al. 2019, 2020; G. Raaijmakers et al. 2021; N. Rutherford et al. 2024; L. Mauviard et al. 2025; M. Hoogkamer et al. 2026). Here, we only provide a brief overview of this framework.

N<sub>EO</sub>ST builds EOSs compatible with theoretical constraints at low densities. At densities up to  $0.5n_0$ , we use the Baym-Pethick-Sutherland (BPS) crust EOS (G. Baym et al. 1971). The region  $0.5n_0 < n \leq 1.5n_0$  is described by a probability distribution derived from  $\chi$ EFT calculations of dense matter, covered in detail in Section 3. The transition from BPS to  $\chi$ EFT is realized via linear interpolation from the last point in the crust to the first point of the  $\chi$ EFT EOS with an equal or higher pressure and density. Two different general high-density extensions are used beyond  $1.5n_0$ : a piecewise-polytropic (PP) (J. S. Read et al. 2009; K. Hebeler et al. 2013) or a speed-of-sound (CS) model (S. K. Greif et al. 2019), both with the same parameter ranges as in N. Rutherford et al. (2024) for the transition density  $1.5n_0$ . The PP model has three segments of the form  $P(n) = K(n/n_0)^\Gamma$ , with  $\Gamma_1, \Gamma_2 \in [0, 8]$ ,  $\Gamma_3 \in [0.5, 8]$ , where the first polytrope goes from  $1.5n_0$  to  $n_1 \in [2, 8.3]n_0$ , the second segment from  $n_1$  to  $n_2 \in [2, 8.3]n_0$ , and the third from  $n_2$  to the maximal central density. The CS model is given by (in units where the speed of light  $c = 1$ )

$$c_s^2(x) = a_1 e^{-\frac{1}{2}(x-a_2)^2/a_3^2} + a_6 + \frac{\frac{1}{3} - a_6}{1 + e^{-a_5(x-a_4)}}, \quad (1)$$

where  $c_s^2 = dP/d\varepsilon$ ,  $x = \varepsilon/(m_N n_0)$ , and the nucleon mass  $m_N = 939.565$  MeV. The parameters vary within the ranges of  $a_1 \in [0.1, 1.5]$ ,  $a_2 \in [1.5, 12]$ ,  $a_3/a_2 \in [0.05, 2]$ ,  $a_4 \in [1.5, 37]$ ,  $a_5 \in [0.1, 1]$ , and  $a_6$  continuously matches to the  $\chi$ EFT EOS. As described in Section 4, all EOSs are checked for pQCD compatibility and, in case of failure, pQCD-compatible extensions are built. This ensemble of EOSs forms our prior,  $p(\boldsymbol{\theta}|\mathbb{M})p(\varepsilon|\boldsymbol{\theta}, \mathbb{M})$ , where  $\mathbb{M}$  represents the EOS models,  $\boldsymbol{\theta}$  its parameters, and  $\varepsilon$  its central energy densities.

<sup>1</sup> <https://github.com/xpsi-group/neost>

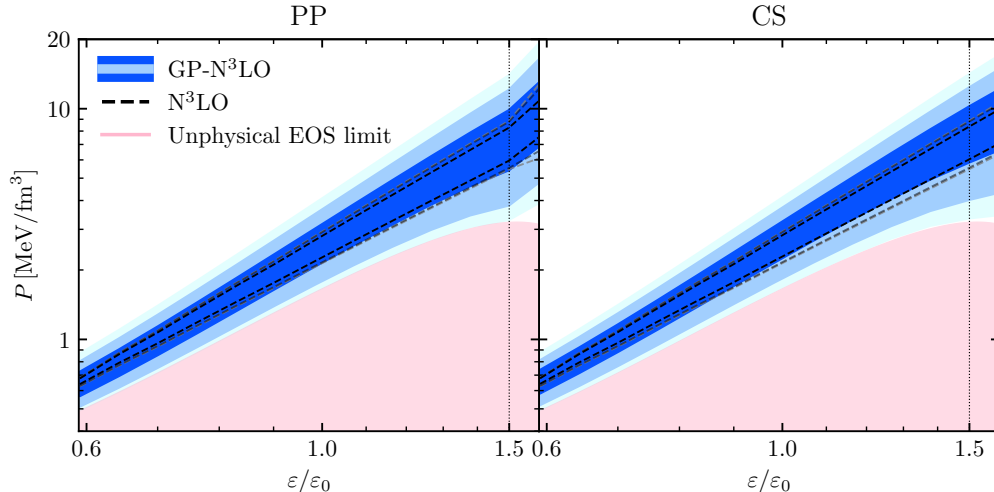


**Figure 1.** Pressure-energy density prior distributions for the PP (left panel) and CS (right panel) extensions with Bayesian  $\chi$ EFT uncertainties up to  $1.5n_0$  (GP-N<sup>3</sup>LO, blue regions) and uniformly sampled in the previous N<sup>3</sup>LO range (N<sup>3</sup>LO, black dashed lines). The dark (light, lighter) blue regions and dashed black (grey, lighter grey) lines encompass the 68% (95% and 99.7%) credible intervals for the GP-N<sup>3</sup>LO and N<sup>3</sup>LO cases, respectively. The pink region shows all EOSs excluded from the prior for their unphysical behavior above  $1.5\varepsilon_0$ , indicated by the vertical thin dotted line.

NEoST uses Bayesian inference to find the most likely EOSs to describe given astrophysical data. Hence, with Bayes’ theorem, the posterior distributions of the EOS can be written as

$$\begin{aligned}
 p(\boldsymbol{\theta}, \varepsilon \mid \mathbf{d}, \mathbb{M}) &\propto p(\boldsymbol{\theta} \mid \mathbb{M}) p(\varepsilon \mid \boldsymbol{\theta}, \mathbb{M}) \\
 &\times \prod_i p(\Lambda_{1,i}, \Lambda_{2,i}, q_i \mid \mathcal{M}_c, \mathbf{d}_{\text{GW},i}) \\
 &\times \prod_l p(M_l, R_l \mid \mathbf{d}_{\text{NICER+radio},l}), \quad (2)
 \end{aligned}$$

where  $\mathbf{d}$  represents the selected dataset,  $\Lambda_{1,i}$  and  $\Lambda_{2,i}$  are the tidal deformabilities associated with the GW data  $\mathbf{d}_{\text{GW},i}$ , and  $\mathbf{d}_{\text{NICER+radio},l}$  are the mass-radius ( $M_l$ - $R_l$ ) NICER data already combined with constraints from radio observations. As discussed in G. Raaijmakers et al. (2021), we fix the neutron star binaries’ chirp mass,  $\mathcal{M}_c$ . Our setup for the EOS parameters takes largely the same form as detailed in N. Rutherford et al. (2024) and further used in L. Mauviard et al. (2025), with two improvements explained in detail in Sections 3 and 4. The astrophysics data entering the likelihood are as in L. Mauviard et al. (2025) and described in Section 5.1.

The EOS parameters are sampled using the nested sampling algorithm (J. Skilling 2004) implemented in MULTINEST (F. Feroz et al. 2009; J. Buchner et al. 2014) using 5,000 (100,000) live points for calculating posteriors (priors). As of v2.2.0, NEoST utilizes the MPI multiprocessing feature of MULTINEST, which substantially decreases the wall time of the sampling. MPI is further used in the postprocessing step of converting the

EOS parameter samples to distributions of  $M$ ,  $R$ ,  $P$ ,  $\varepsilon$ ,  $c_s^2$ , and other EOS representations.

### 3. BAYESIAN $\chi$ EFT UNCERTAINTIES USING A GAUSSIAN PROCESS

Around nuclear saturation density, our EOS prior is based on order-by-order  $\chi$ EFT calculations of asymmetric nuclear matter by J. Keller et al. (2023) using the N<sup>3</sup>LO two- and three-nucleon (NN+3N) interaction with cutoff 450 MeV (D. R. Entem et al. 2017; C. Drischler et al. 2019). We consider a Bayesian approach to quantify truncation uncertainties of the EFT expansion, as introduced in C. Drischler et al. (2020a,b), implemented by a two-dimensional GP in H. Götting et al. (2025) that accounts for correlations along density and proton fraction. Here and in the following we label our results obtained with this  $\chi$ EFT prior as “GP-N<sup>3</sup>LO”. We compare this EOS description to our previously used non-Bayesian model, known as the EKM prescription (E. Epelbaum et al. 2015), where the truncation uncertainty is estimated by inspecting expansion coefficients at lower orders and adopting the largest relative correction as the truncation error. We refer to results obtained with this method as “N<sup>3</sup>LO”.

In our previous works (N. Rutherford et al. 2024; L. Mauviard et al. 2025), we used the latter N<sup>3</sup>LO priors and assumed that the EOS was uniformly distributed in pressure-energy density ( $P$ - $\varepsilon$ ) space within the limits of the EKM prescription. Here, we improve on this by letting the EOS follow the normal distribution defined by the GP with given mean and covariance functions

from H. Götting et al. (2025). When drawing a sample from the GP representation of the pressure, we have to guarantee that it is monotonically increasing. This is not guaranteed for random samples drawn from the GP in the standard way. We ensure monotonicity by drawing  $x$  from a normal distribution  $\propto \exp(-x^2/2)$  to define a draw from the GP-N<sup>3</sup>LO distribution according to

$$P_{\text{sample}}(n) = P_{\mu}(n) + x \cdot P_{\sigma}(n), \quad (3)$$

where  $P_{\mu}(n)$  is the GP mean for matter in  $\beta$ -equilibrium at density  $n$  and  $P_{\sigma}(n)$  the standard deviation. The resulting GP-N<sup>3</sup>LO priors are shown in Figure 1. At the 68% credible interval, they are similar to the EKM prescription for the N<sup>3</sup>LO band, but the tails of the GP uncertainties allow for broader pressure ranges.

As the truncation uncertainty encoded in the standard deviation is also a function of the density, it grows faster than the pressure itself at the tail of the distribution. Specifically for the lower end of the pressure probability at densities approaching  $1.5\varepsilon_0$  (where  $\varepsilon_0$  is the energy density at saturation), this behavior causes unphysical samples, with decreasing pressures. We exclude those samples before creating the high-density EOS extension. For GP-N<sup>3</sup>LO, this corresponds to assigning zero sampling probability to about 7% of the EOSs at the lower pressure end of the populated interval of the distribution. This excludes the pink region in Figure 1 from the sampled GP-N<sup>3</sup>LO distribution. As a result, the 68% region is slightly shifted to higher pressures for GP-N<sup>3</sup>LO versus N<sup>3</sup>LO.

#### 4. ENFORCING PQCD COMPATIBILITY

We implement the compatibility with pQCD calculations at very high densities following the procedure described in O. Komoltsev & A. Kurkela (2022)<sup>2</sup> and first employed in T. Gorda et al. (2023b). In N<sup>3</sup>LO, we check all EOSs with the PP or CS extensions for pQCD compatibility. For this procedure, a grid of EOS pressure-energy density points is checked on whether they could reach the calculated pQCD limits in a causal and thermodynamically consistent way. If one of these points fails the pQCD check before reaching the maximum stable neutron star central energy density, a pQCD-compatible extension is built from the last pQCD-compatible EOS pressure-energy density point on. This extension follows a “minimum” or “maximum” scenario, depending on whether the point failed the pQCD check because its pressure exceeded the upper

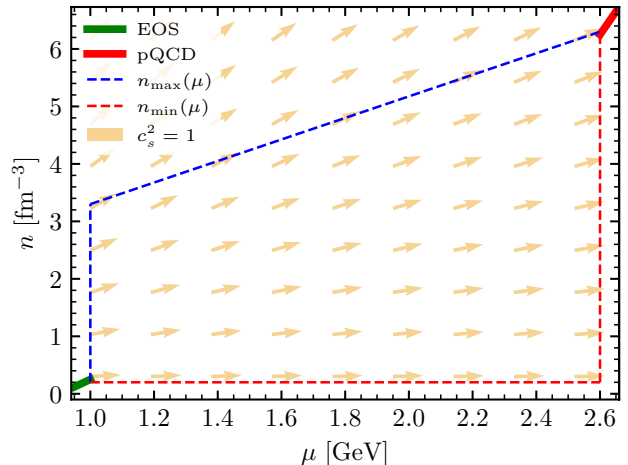


**Figure 2.** Visual representation of the “minimum” (red dashed line) and “maximum” (blue dashed line) pQCD-compatible extensions to an EOS (green) in the number density–chemical potential ( $n$ – $\mu$ ) plane. The pQCD limit is in red. Orange arrows indicate the  $c_s^2 = 1$  lines.

or lower limit of the allowed pressure range. These extensions are illustrated in Figure 2 in the  $n$ – $\mu$  plane. The pressure is connected to the  $n$ – $\mu$  plane by the pressure difference  $\Delta P = \int_{\mu_{\text{EOS}}}^{\mu_{\text{pQCD}}} n(\mu) d\mu$  between the last EOS point (green) and the first point of the pQCD limit (red). The red dashed line indicates the “minimum” extension scenario, where a luminal ( $c_s^2 = 1$ ) EOS is built from the last pQCD-compatible EOS point until the baryon chemical potential  $\mu = 2.6$  GeV, then a phase transition in the  $n$ – $\mu$  plane is realized to the pQCD limit. The blue dashed line represents the “maximum” extension scenario, where the order of these processes is reversed and the phase transition is built first, then a luminal EOS connects to the pQCD limit.

The red pQCD limit shown in Figure 2 was derived in T. Gorda et al. (2021a,b). Since the uncertainty of the pQCD calculations is dominated by truncation errors of the perturbative expansion, the results are dependent on the choice of renormalization scale  $\Lambda$ . To estimate this uncertainty, we work with the dimensionless renormalization scale  $X = \frac{3\Lambda}{2\mu}$  and sample  $X$  values according to a log-uniform distribution in the interval  $[0.5, 2]$ , following the scale averaging discussed in T. Gorda et al. (2023b). The baryon chemical potential  $\mu$  is fixed at 2.6 GeV (T. Gorda et al. 2023b; E. S. Fraga et al. 2014). At this value, the relative uncertainty turns out to be about  $\pm 25\%$  around the mean value.

Including the pQCD extension during the EOS construction broadens the priors in the  $P$ – $\varepsilon$  and  $M$ – $R$  spaces. In particular, a significant number of soft EOSs are made compatible with the pQCD limit through

<sup>2</sup> Code available at <https://github.com/OKomoltsev/QCD-likelihood-function>

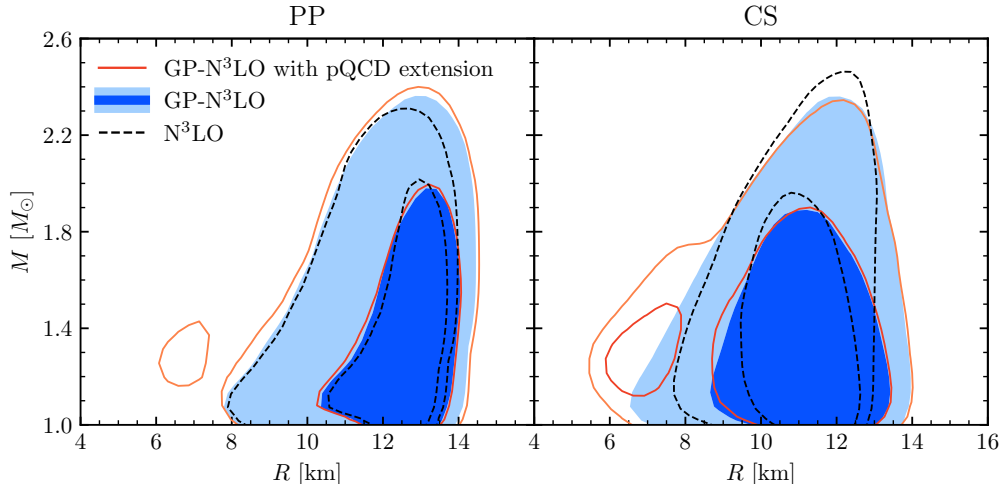


**Figure 3.** Mass-radius prior distributions for the PP (left panel) and CS (right panel) extensions with Bayesian  $\chi$ EFT uncertainties up to  $1.5n_0$  without pQCD extensions (GP-N<sup>3</sup>LO, blue regions), with pQCD extensions (GP-N<sup>3</sup>LO with pQCD extension, solid red and orange lines), and uniformly sampled in the previous N<sup>3</sup>LO range (N<sup>3</sup>LO, black dashed lines). The dark (light) blue regions, the solid red (orange), and the inner (outer) black dashed lines encompass the 68% (95%) credible intervals. The regions at radii  $R \lesssim 8$  km in the orange/red contours are a result of softer EOSs being included in the prior by the pQCD extensions.

“minimum” extensions, generating neutron stars with relatively low masses and radii (around  $R \lesssim 8$  km and  $M \lesssim 1.6 M_\odot$ ), as can be seen in Figure 3. This is present when either GP-N<sup>3</sup>LO or N<sup>3</sup>LO EOSs are used (the latter is not shown). “Maximum” extensions are also present for stiffer EOSs, but they do not change the  $P$ - $\varepsilon$ ,  $M$ - $R$ , or the maximum TOV mass-radius ( $M_{\text{TOV}}-R_{\text{TOV}}$ ) prior distributions significantly, as the corresponding pQCD-incompatible points are already close to the maximum neutron star central densities. Thus, except for the excess at relatively low masses and radii, the impact of the pQCD extension is minor. As we will see, because these low masses and radii are excluded by astrophysical observations, the impact of the pQCD extension will become negligible for the posteriors.

## 5. RESULTS OF EOS INFERENCE

In this section, we investigate the impact of the new GP-based  $\chi$ EFT prior and pQCD-extensions on the EOS posteriors in the pressure-energy density, mass-radius, and speed-of-sound planes. We also infer the  $L$  parameter, i.e., the slope of the symmetry energy, from astrophysical observations.

### 5.1. Astrophysical data

Our input astrophysics data consist of four NICER pulsars and two gravitational wave events from LIGO/Virgo. The pulsars, with their pulse profile modeling (PPM) configurations given in parentheses, are PSR J0740+6620 (ST-U) (T. Salmi et al. 2024a), PSR

J0030+0451 (ST+PDT) (S. Vinciguerra et al. 2024)<sup>3</sup>, PSR J0437-4715 (CST+PDT) (D. Choudhury et al. 2024), and PSR J0614-3329 (ST+PDT) (L. Mauviard et al. 2025). For the first three we employ the same configurations as in L. Mauviard et al. (2025) and for PSR J0614-3329 we employ the headline result. Mass constraints from radio observations are included in the data in the cases of J0437, J0740, and J0614. In addition to the NICER data, we include the tidal deformabilities  $\Lambda_1$ ,  $\Lambda_2$  and mass ratio  $q$  of the two components of the gravitational wave events GW170817 (B. P. Abbott et al. 2019) and GW190425 (B. P. Abbott et al. 2020).

### 5.2. Mass-radius posteriors

Figure 4 reveals that the pQCD constraints have a negligible impact on the mass-radius posteriors for both PP and CS extensions. This shows that most of the EOSs included by pQCD extensions in the prior—primarily very soft EOSs—are excluded by the astrophysical data in the posterior. In particular, the presence of the high-mass pulsar J0740 disfavors these softer EOSs, explaining the disappearance of the EOSs at  $R \lesssim 8$  km and  $M \lesssim 1.6 M_\odot$  in the prior (see Figure 3).

The new GP-based  $\chi$ EFT prior accommodates a wider range of EOSs in the low-density regime around sat-

<sup>3</sup> This analysis has recently been superseded by Y. Kini et al. (2026), which uses a larger NICER data set together with XMM data, and improved sampler settings. The results found in the newer study are however highly compatible with the ST+PDT results from S. Vinciguerra et al. (2024).

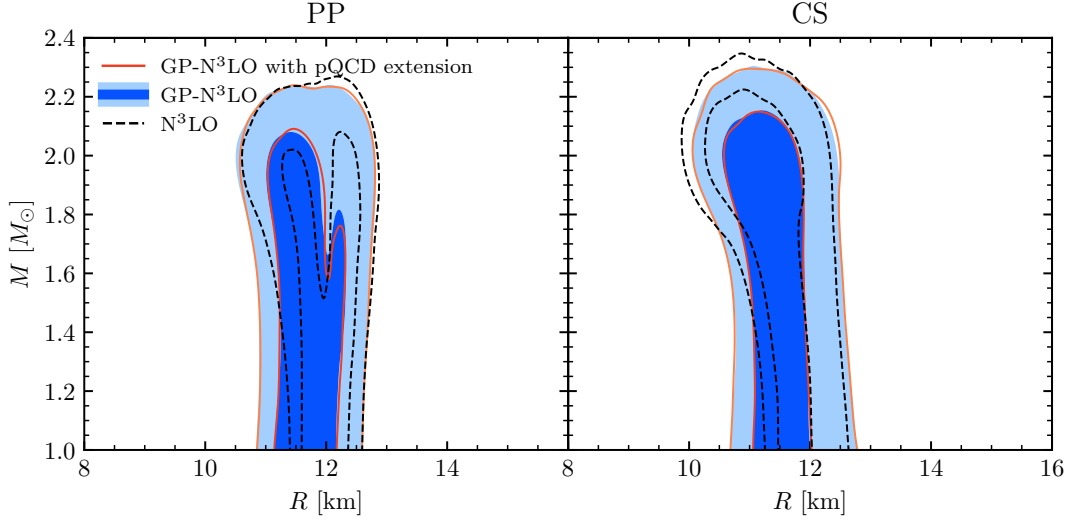


**Figure 4.** Same as Figure 4 but for the mass-radius posterior distributions.

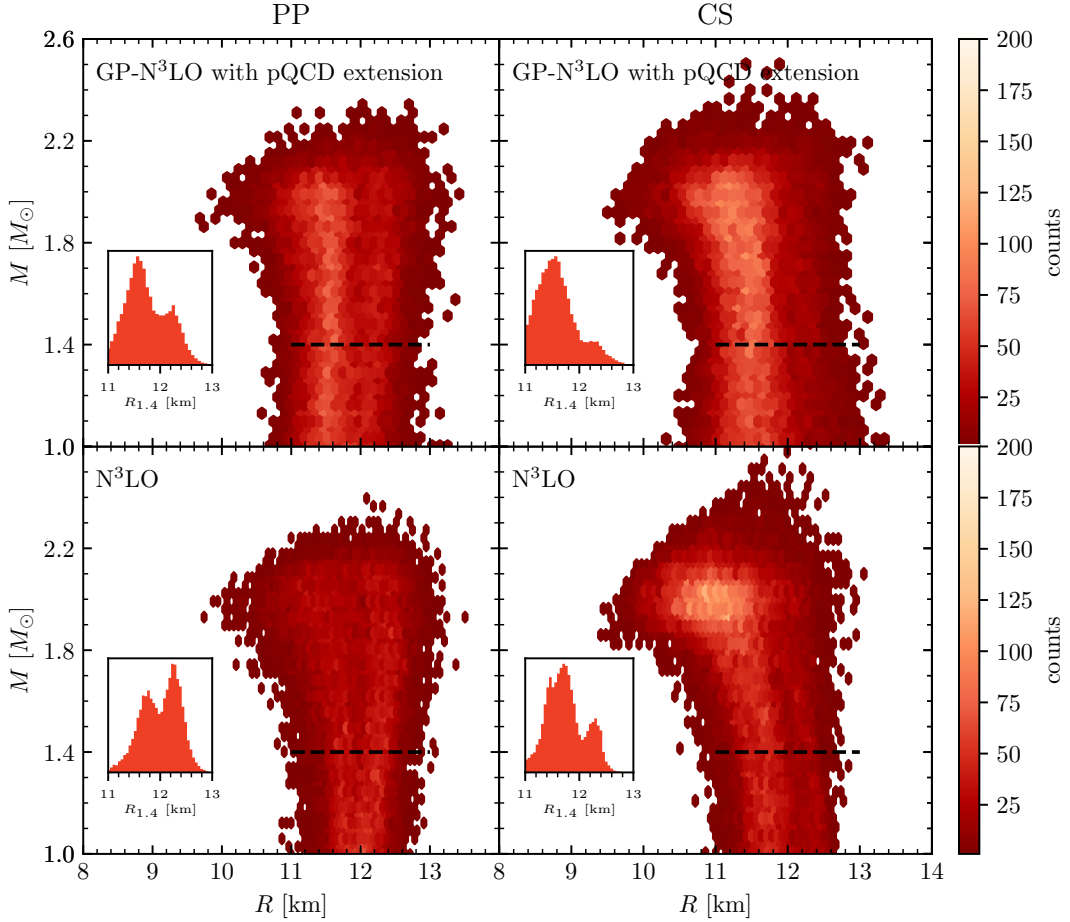


**Figure 5.** Mass-radius posterior distributions showing the 2D histogram for the PP (left panel) and CS (right panel) extensions with Bayesian  $\chi$ EFT uncertainties up to  $1.5m_0$  with pQCD extensions (GP-N<sup>3</sup>LO with pQCD extension, upper panels) and uniformly sampled in the previous N<sup>3</sup>LO range (N<sup>3</sup>LO, lower panels). The dark shaded hexagons indicate a lower number of mass-radius samples, while the lighter shaded hexagons indicate a higher number of mass-radius samples. The insets show the radius distribution for a  $1.4 M_\odot$  star, indicated by the black dashed lines.

uration density than the uniformly distributed prior

we have used in earlier works. It is therefore natu-

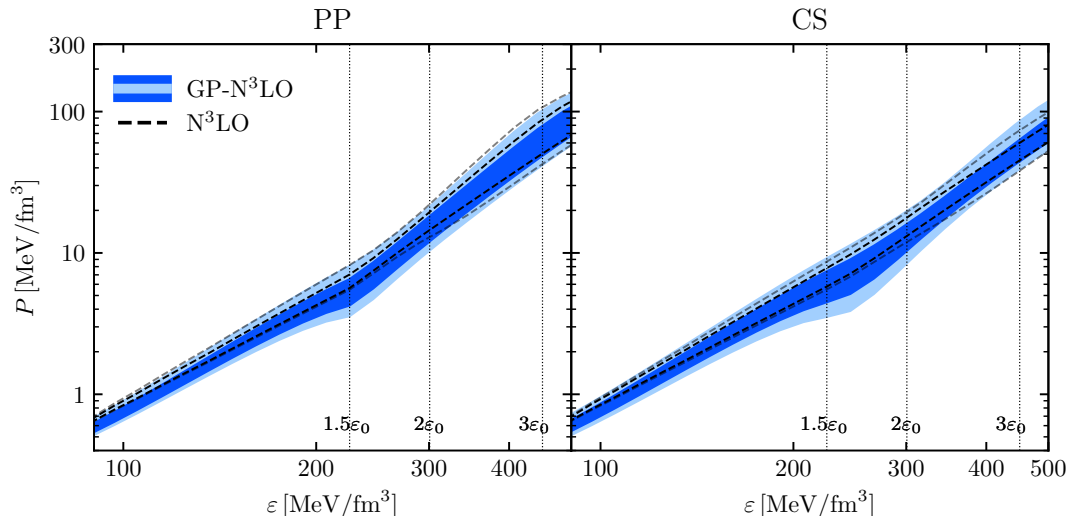


**Figure 6.** Pressure-energy density posterior distributions for the PP (left panel) and CS (right panel) extensions with Bayesian  $\chi$ EFT uncertainties up to  $1.5n_0$  with pQCD extensions (GP-N<sup>3</sup>LO, blue regions) and uniformly sampled in the previous N<sup>3</sup>LO range (N<sup>3</sup>LO, black dashed lines). The dark (light) blue regions and the inner (outer) black dashed lines encompass the 68% (95%) credible intervals. The vertical thin lines mark the points of  $1.5, 2$  and  $3\epsilon_0$  for easier reference.

ral to expect wider posterior distributions, which we indeed observe. Figure 4 shows that the mass-radius posteriors with GP-N<sup>3</sup>LO encompass a somewhat wider range to lower radii for stars in the mass range  $1.0 - 1.6 M_\odot$ . At higher masses, the posteriors are largely unchanged: The PP GP-N<sup>3</sup>LO shifts weight slightly to low-radius high-mass stars, while the CS GP-N<sup>3</sup>LO posterior slightly to high-radius high-mass stars.

Figure 5 shows the same results as Figure 4, but as two-dimensional histograms rather than credible intervals. This reveals some structure in the posteriors that is obscured in the plotting style of Figure 4. In particular, the bimodal-like structure around  $1.4 M_\odot$  and heavier masses, previously seen in N. Rutherford et al. (2024) and L. Mauviard et al. (2025), is also present here. This structure is also visible to an extent in the left panel of Figure 4. This effect, where the posterior at  $R \approx 12$  km has a dip compared to both smaller and greater radii, may arise as a combination of stiffer priors and soft-favoring data (GW170817, J0614, and J0437) in combination with high-mass neutron stars with masses  $M \geq 2M_\odot$  (like J0740).

### 5.3. Pressure-density posteriors

In Figures 6 and 7, the new  $P$ - $\epsilon$  posteriors show a significant broadening to lower pressures below  $2\epsilon_0$  as a direct result of using the GP-N<sup>3</sup>LO  $\chi$ EFT. The upper limit of the posteriors is mostly unaffected, indicating that the astrophysical data already favor lower pressures around saturation density. This is clearly seen at  $1.0\epsilon_0$  in the leftmost panel of Figure 7, where the upper parts of the GP-N<sup>3</sup>LO and N<sup>3</sup>LO distributions are

nearly identical, whereas lower pressures are cut off in the N<sup>3</sup>LO case. This effect, and the square shape of the prior for N<sup>3</sup>LO, are due to the uniform EOS sampling within the more restricted EKM limits. Nonetheless, beyond twice nuclear saturation density, the effect of the  $\chi$ EFT prior becomes very small.

Most importantly, within our broad prior ranges, we observe a clear stiffening of the EOS at  $\epsilon \gtrsim 3\epsilon_0$ , from favoring softer parts of the prior to favoring stiffer parts in Figure 7. Similarly to the effects in the  $M$ - $R$  plane, discussed in the previous section, including pQCD-compatible extensions only slightly broadens the  $P$ - $\epsilon$  priors, allowing for softer EOSs, and does not alter the posteriors visibly. We also note that the effect of the high-density extension (PP versus CS) is overall minor, with PP just showing a slight preference for higher pressures at  $2 - 4\epsilon_0$ .

### 5.4. Speed of sound posteriors

Figure 8 shows the speed of sound at  $1, 1.5, 2, 3$  and  $4\epsilon_0$  corresponding to the pressures in Figure 7. Above saturation density, the GP- $\chi$ EFT prior allows for more weight at lower speeds of sound around nuclear saturation density. Also here we observe a clear stiffening of the EOS between  $2 - 3\epsilon_0$ , with speeds of sound changing from mostly below the conformal limit,  $c_s^2 = 1/3$ , at  $2\epsilon_0$  to mostly above at  $3\epsilon_0$ . While the posterior speed of sound range is similar for the PP and CS high-density extensions, the distributions are more different than for the pressure, especially at  $4\epsilon_0$ . This is natural with the speed of sound being a derivative of the pressure. Also the differences of the GP-N<sup>3</sup>LO and N<sup>3</sup>LO cases are

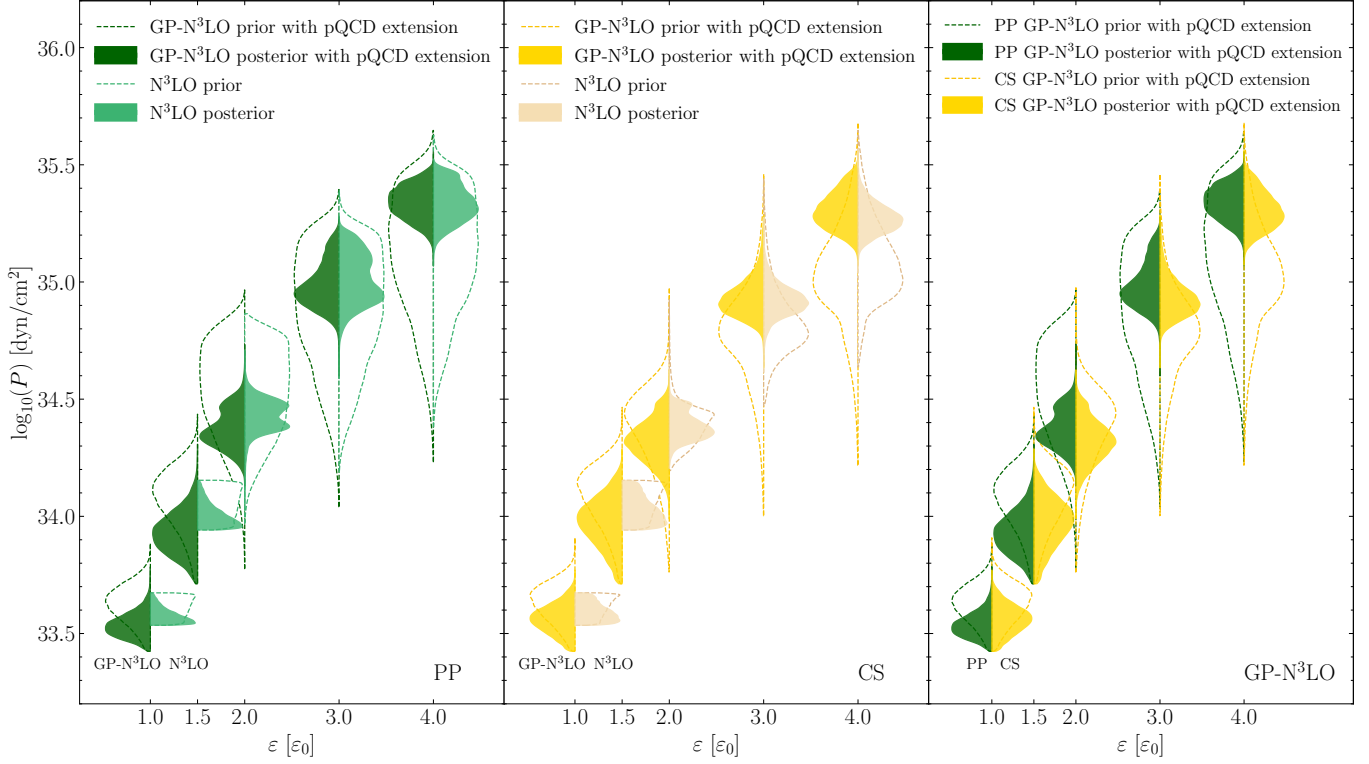


**Figure 7.** Prior (dashed lines) and posterior distributions (filled contours) for the pressure at 1, 1.5, 2, 3 and  $4\epsilon_0$  with Bayesian  $\chi$ EFT uncertainties up to  $1.5n_0$  with pQCD extensions (GP-N<sup>3</sup>LO) versus uniformly sampled (N<sup>3</sup>LO) for the PP extension (left panel), CS extension (middle panel), and a comparison between PP and CS extensions for GP-N<sup>3</sup>LO (right panel).

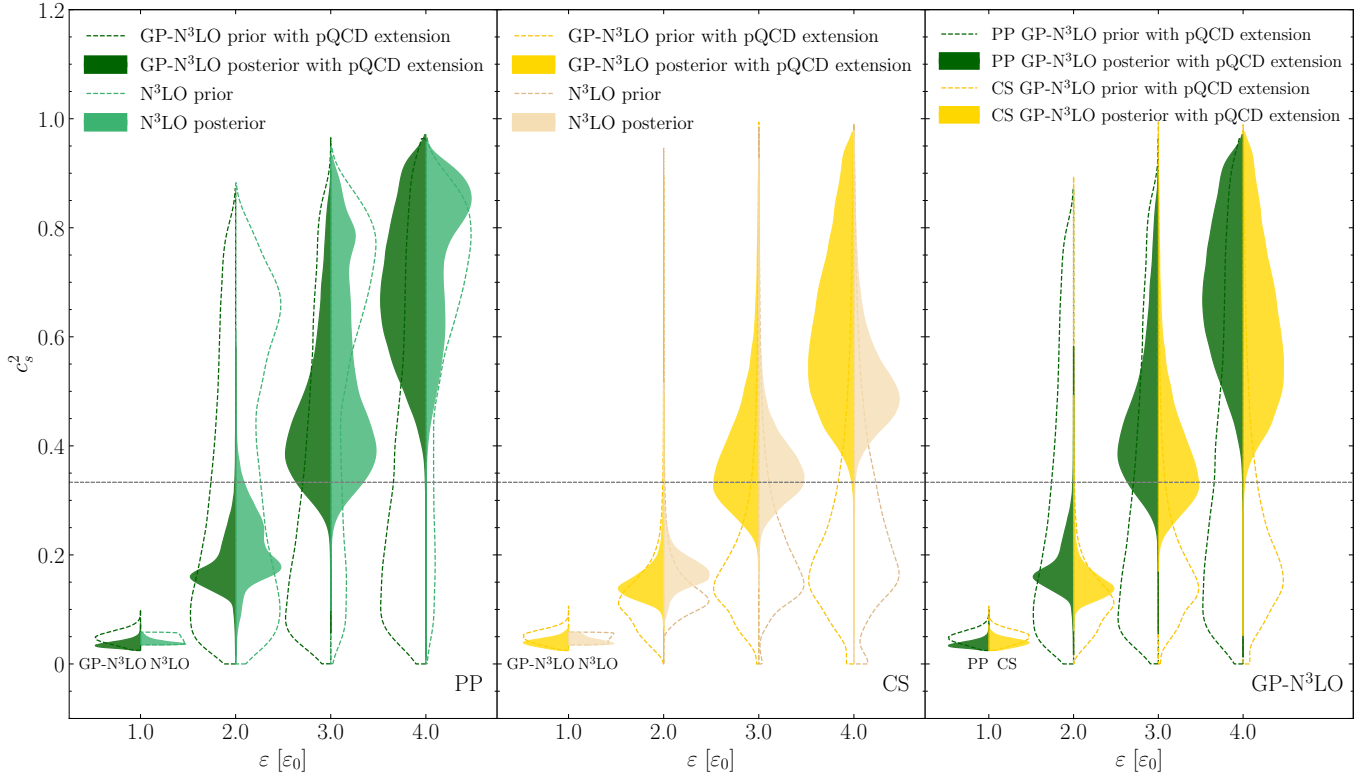


**Figure 8.** Same as Figure 7 but for the speed of sound. The horizontal black dashed line shows the conformal limit ( $c_s^2 = 1/3$ ).

as expected from the pressure: while both have similar

ranges, the GP-N<sup>3</sup>LO has more weight towards lower speeds of sound.

**Table 1.** Prior and posterior credible intervals (68% and 95%) for the  $L$  parameter based on the GP- $N^3$ LO EOS with the PP and CS extensions. In addition to the posterior ranges for the full LIGO/Virgo (GW170817 and GW190425) and NICER (J0740, J0437, J0614, and J0030), labeled “Posterior”, we also give the ranges for the other astrophysics data scenarios considered in Figure 10.

Data scenario	L [MeV] (PP)		L [MeV] (CS)	
	68%	95%	68%	95%
Prior	48.0 – 67.2	40.5 – 75.9	49.0 – 69.0	40.5 – 76.5
Posterior	42.6 – 52.0	40.0 – 58.6	44.2 – 56.7	39.5 – 62.6
J0740	51.0 – 66.3	45.6 – 74.7	54.1 – 72.9	45.2 – 80.4
J0740+J0437	47.1 – 60.4	43.2 – 68.9	48.9 – 66.0	42.0 – 73.8
J0740+GW170817	50.1 – 62.0	44.8 – 69.0	52.5 – 68.3	43.4 – 74.0
J0740+J0437+J0614+GW170817	43.1 – 53.3	40.0 – 60.2	43.5 – 56.3	39.5 – 63.5

While both PP and CS extensions allow for first-order phase transitions (with  $c_s^2 = 0$  regions), the astrophysical data disfavor these for the densities shown in Figure 8, as can be seen by the absence of a posterior excess at  $c_s^2 = 0$ . This is consistent with previous findings [see, for example, the previous study including both  $\chi$ EFT and pQCD constraints (T. Gorda et al. 2023a)].

### 5.5. Inferring the $L$ parameter

With the sampled GP- $N^3$ LO distribution up to  $1.5n_0$ , we can also infer the  $L$  parameter of the EOS. The  $L$  parameter characterizes the slope of the symmetry energy at saturation density  $L = 3n_0 \left. \frac{\partial S(n)}{\partial n} \right|_{n=n_0}$  and is thus related to the pressure of pure neutron matter. Given that neutron star matter and pure neutron matter are highly correlated—the correlation length of the two-dimensional GP in the proton-fraction ( $x$ ) direction is  $l_x = 0.31$  (H. Götting et al. 2025)—we can easily translate a draw from our normally sampled  $\chi$ EFT EOS for neutron star matter back to pure neutron matter by assuming they are fully correlated in the proton-fraction direction.

In Figure 9, we show the prior and posterior distributions for the GP- $N^3$ LO EOS. The prior distributions reflect the  $\chi$ EFT uncertainties for the  $L$  parameter based on the two-dimensional GP for the chiral NN+3N interaction used (H. Götting et al. 2025), and are thus identical for the PP and CS extensions except for the sampling statistics. The  $L$  parameter ranges are consistent with the range for different chiral EFT interactions from F. Alp et al. (2025) given by 41.2 – 67.3 MeV. Note that the latter range does not include EFT truncation uncertainties, which make up the sampled GP- $N^3$ LO distribution based on the considered  $N^3$ LO NN+3N interaction (D. R. Entem et al. 2017; C. Drischler et al. 2019). As

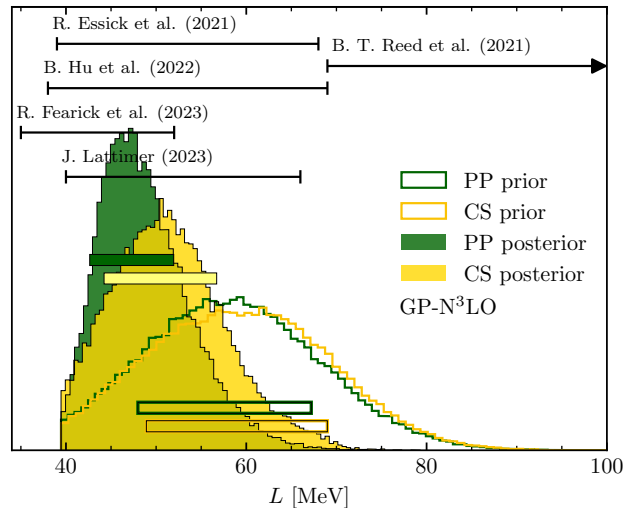


**Figure 9.** Prior (unfilled) and posterior (filled) distributions for the  $L$  parameter based on the GP- $N^3$ LO EOS with the PP (green) and CS (yellow) high-density extensions. The posterior distributions include all astrophysics data considered in this work. We also give the 68% credible interval as colored horizontal bars (unfilled prior and filled posterior), as well as comparisons to previous  $L$  ranges (for details see text, all intervals are 68% except for R. W. Fearick et al. (2023), which is based on a set of NN+3N interactions). The upper extent of B. T. Reed et al. (2021) is 143 MeV.

shown by the limit of  $L \gtrsim 39.5$  MeV in Figure 9, for lower  $L$  parameters our GP- $N^3$ LO EOS would lead to an unphysical EOS with a decreasing pressure at  $1.5n_0$  (see the discussion in Section 3).

Our results for the posterior distributions for all astrophysics data are only weakly dependent on the high-density PP or CS extension, with the CS posterior extending to somewhat larger  $L$ . At the 68% credible in-

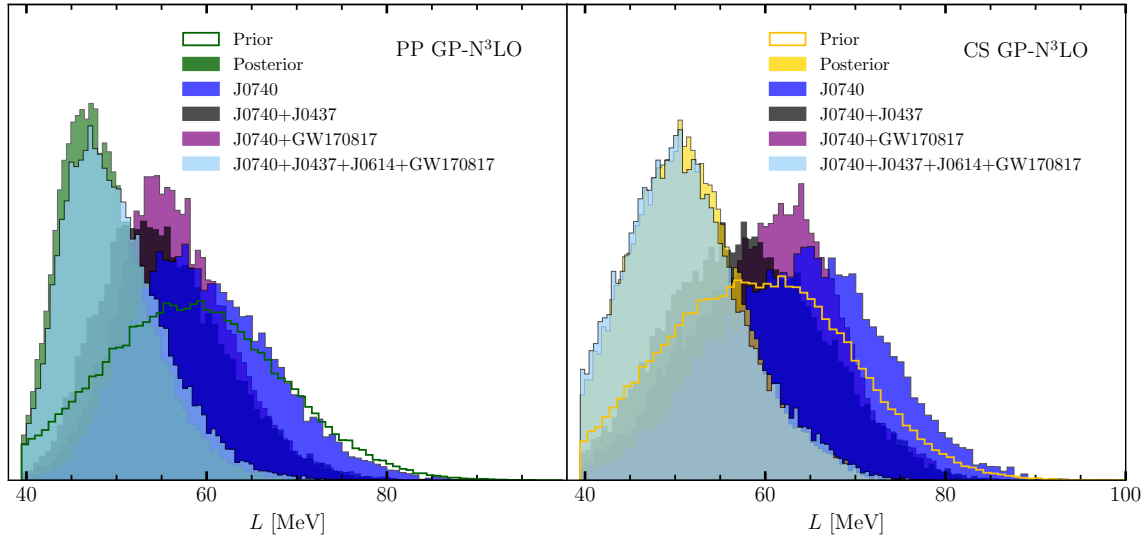


**Figure 10.** Distributions for the  $L$  parameter for the GP- $N^3$ LO EOS with the PP (left) and CS (right) high-density extensions, as in Figure 9, but based on different astrophysics data scenarios specified in the legend (for details see text).

terval, we find the ranges for  $L$  to be 42.6 – 52.0 MeV (PP) and 44.2 – 56.7 MeV (CS), preferring lower ranges than our priors. All 68% and 95% ranges for  $L$  are also given in Table 1. As shown in Figure 9, our posterior ranges for  $L$  are also consistent with other astrophysics and/or  $\chi$ EFT informed ranges from R. Essick et al. (2021); B. Hu et al. (2022); R. W. Fearick et al. (2023); J. M. Lattimer (2023), but we generally find stronger constraints from all astrophysics data considered in this work. Only the larger  $L$  values obtained purely from PREX prefer larger  $L$  values (B. T. Reed et al. 2021), but also have very large uncertainties.

Finally, we show in Figure 10 the posterior distributions for  $L$  obtained from different astrophysics data scenarios. This shows that the full astrophysics posterior is dominated by the combined data from “J0740+J0437+J0614+GW170817”, while subsets of these observations are prior-dominated and lead to a broader  $L$  posterior extending to higher  $L$  values. We thus expect the updated results for J0030 from Y. Kini et al. (2026) to not significantly alter our posteriors. However, upcoming mass-radius contours from high-mass pulsar PSR J1614-2230 could have an interesting impact. In particular, a smaller (larger) radius for this source than J0740 could pull  $L$  to lower (larger) values, making this astrophysics information interesting for our analysis. We also studied the impact of including only the GW170817 or only the J0614 data, which also shifts the  $L$  prior to smaller values, but both of these scenarios still present a significant overlap with the prior up to  $L \approx 80$  MeV.

## 6. SUMMARY AND CONCLUSIONS

In this paper, we have studied the effects of two new developments for astrophysical EOS inferences: Bayesian  $\chi$ EFT uncertainty quantification and the incorporation of pQCD constraints. Using the GP from H. Götting et al. (2025) to model the  $\chi$ EFT truncation uncertainties, we have built an EOS distribution around nuclear saturation density with a clear statistical interpretation. The GP allows for a significantly broader range of pressures up to about  $1.5n_0$  compared to our previous works. The resulting distributions include softer EOSs, while stiffer EOSs are disfavored by the astrophysical data. This led to a slight broadening of the  $M$ – $R$  posterior to lower radii for neutron stars with  $1.0 - 1.6 M_\odot$ .

The enforcement of pQCD-compatibility at extremely high densities following O. Komoltsev & A. Kurkela (2022) led to the inclusion of very soft EOSs in the prior. This was most notable in the  $M$ – $R$  prior, which exhibits a significant probability for low-mass stars with radii below 8 km, whereas these stars were not included in the PP and CS ensembles before. However, the effects of the pQCD constraints on the posteriors were found to be negligible, as the vast majority of EOSs that are included through pQCD extensions are ruled out by the astrophysical data, mainly from the high-mass pulsar J0740.

Most interestingly for the EOS, we have found a clear stiffening of the pressure at  $\varepsilon \gtrsim 3\varepsilon_0$ , from favoring softer pressures at lower  $\varepsilon$  to favoring stiffer EOSs above. This clear stiffening of the EOS between  $2 - 3\varepsilon_0$  was also seen in the speed of sound, with speeds of sound changing

from mostly below the conformal limit,  $c_s^2 = 1/3$ , at  $2\epsilon_0$  to mostly above at  $3\epsilon_0$ .

The strong correlation between pure neutron matter and matter in beta equilibrium has allowed us to also infer the symmetry energy slope parameter  $L$  from astrophysics. For the 68% credible interval, we obtained  $L = 42.6 - 52 \text{ MeV}$  and  $L = 44.2 - 56.7 \text{ MeV}$ —in the lower ranges of the prior—using the PP and CS extensions, respectively. Our findings are consistent with other theoretical and experimental inferences of the  $L$  parameter, but our credible intervals are substantially narrower. Moreover, we have found that the  $L$  posterior is mainly driven by the combination of GW170817 LIGO/Virgo and J0740, J0437, J0614 NICER data.

LIGO/Virgo continues to gather data on GWs, and several other neutron star and GW observatories, such as Cosmic Explorer (D. Reitze et al. 2019), Einstein Telescope (M. Punturo et al. 2010), NewAthena (M. Cruise et al. 2025) and eXTP (A. Li et al. 2025), are planned for the next decade. In addition, new radio facilities such as SKA (A. Basu et al. 2025) promise important advances on the measurement of neutron star masses and moments of inertia. Upcoming data from these facilities will greatly increase our understanding of compact stars and the dense matter EOS. Our work shows how astrophysical data can directly inform the EOS behavior and nuclear matter parameters like  $L$ . These exciting prospects open up several avenues for future research, such as identifying whether compact star data EOS constraints are in agreement with laboratory data (R. Somasundaram et al. 2025). This kind of study also places high demands on theoretical EOS modeling, where all relevant sources of uncertainty need to be rigorously accounted for. Future work needs to also ac-

count for the uncertainties from the many-body method used to calculate the EOS at nuclear densities, see I. Svensson et al. (2026) for initial steps, and from the description of the neutron star crust (H. Göttling et al. 2025). In addition, the agnostic high-density extensions need to be flexible enough to capture all possible EOS behaviors—degrees of freedom and interactions. To this end, GPs trained on various microphysics models (S. Ng et al. 2025) can help to validate that the prior does not bias the results. Finally, an interesting application of this work is to include the GP-N<sup>3</sup>LO in EOS-informed NICER data analysis (M. Hoogkamer et al. 2026).

## 7. ACKNOWLEDGMENTS

We thank Tyler Gorda and Luis Hoff for useful discussions. This work was supported in part by the European Research Council (ERC) under the European Union’s Horizon 2020 research and innovation programme (Grant Agreement No. 101020842) and by the LOEWE Top Professorship LOEWE/4a/519/05.00.002(0014)98 by the State of Hesse. We gratefully acknowledge the computing time provided on the high-performance computer Lichtenberg II at the TU Darmstadt. This is funded by the German Federal Ministry of Education and Research (BMBF) and the State of Hesse. We also gratefully acknowledge the Gauss Centre for Supercomputing e.V. (www.gauss-centre.eu) for providing computing time on the GCS Supercomputer JUWELS at Jülich Supercomputing Centre (JSC). N.R. acknowledges generous support from the Foundational Questions Institute. A.L.W. acknowledges support from NWO ENW-XL grant OCENW.XL21.XL21.038 *Probing the phase diagram of Quantum Chromodynamics*.

## REFERENCES

- Abbott, B. P., Abbott, R., Abbott, T. D., et al. 2019, Properties of the Binary Neutron Star Merger GW170817, *Phys. Rev. X*, 9, 011001, doi: [10.1103/PhysRevX.9.011001](https://doi.org/10.1103/PhysRevX.9.011001)
- Abbott, B. P., Abbott, R., Abbott, T. D., et al. 2020, GW190425: Observation of a Compact Binary Coalescence with Total Mass  $\sim 3.4 M_\odot$ , *Astrophys. J. Lett.*, 892, L3, doi: [10.3847/2041-8213/ab75f5](https://doi.org/10.3847/2041-8213/ab75f5)
- Alp, F., Dietz, Y., Hebeler, K., & Schwenk, A. 2025, Equation of state and Fermi liquid properties of dense matter based on chiral effective field theory interactions, *Phys. Rev. C*, 112, 055802, doi: [10.1103/ls3l-dn1y](https://doi.org/10.1103/ls3l-dn1y)
- Antoniadis, J., Freire, P. C. C., Wex, N., et al. 2013, A Massive Pulsar in a Compact Relativistic Binary, *Sci.*, 340, 1233232, doi: [10.1126/science.1233232](https://doi.org/10.1126/science.1233232)
- Basu, A., Graber, V., Lower, M. E., et al. 2025, Probing Neutron Star Interiors and the Properties of Cold Ultra-dense Matter with the SKA, *Open J. Astrophys.*, 8, 54253, doi: [10.33232/001c.154253](https://doi.org/10.33232/001c.154253)
- Baym, G., Pethick, C., & Sutherland, P. 1971, The Ground state of matter at high densities: Equation of state and stellar models, *Astrophys. J.*, 170, 299, doi: [10.1086/151216](https://doi.org/10.1086/151216)
- Brandes, L., Weise, W., & Kaiser, N. 2023, Inference of the sound speed and related properties of neutron stars, *Phys. Rev. D*, 107, 014011, doi: [10.1103/PhysRevD.107.014011](https://doi.org/10.1103/PhysRevD.107.014011)

- Buchner, J., Georgakakis, A., Nandra, K., et al. 2014, X-ray spectral modelling of the AGN obscuring region in the CDFS: Bayesian model selection and catalogue, *Astron. Astrophys.*, 564, A125, doi: [10.1051/0004-6361/201322971](https://doi.org/10.1051/0004-6361/201322971)
- Chatziioannou, K., Cromartie, H. T., Gandolfi, S., et al. 2025, Neutron stars and the dense matter equation of state, *Rev. Mod. Phys.*, 97, 045007, doi: [10.1103/ymseq-cfw](https://doi.org/10.1103/ymseq-cfw)
- Choudhury, D., Salmi, T., Vinciguerra, S., et al. 2024, A NICER View of the Nearest and Brightest Millisecond Pulsar: PSR J0437–4715, *Astrophys. J. Lett.*, 971, L20, doi: [10.3847/2041-8213/ad5a6f](https://doi.org/10.3847/2041-8213/ad5a6f)
- Cromartie, H. T., Fonseca, E., Ransom, S. M., et al. 2020, Relativistic Shapiro delay measurements of an extremely massive millisecond pulsar, *Nature Astr.*, 4, 72, doi: [10.1038/s41550-019-0880-2](https://doi.org/10.1038/s41550-019-0880-2)
- Cruise, M., Guainazzi, M., Aird, J., et al. 2025, The NewAthena mission concept in the context of the next decade of X-ray astronomy, *Nature Astr.*, 9, 36, doi: [10.1038/s41550-024-02416-3](https://doi.org/10.1038/s41550-024-02416-3)
- Demorest, P., Pennucci, T., Ransom, S., Roberts, M., & Hessels, J. 2010, Shapiro Delay Measurement of A Two Solar Mass Neutron Star, *Nature*, 467, 1081, doi: [10.1038/nature09466](https://doi.org/10.1038/nature09466)
- Dittmann, A. J., Miller, M. C., Lamb, F. K., et al. 2024, A More Precise Measurement of the Radius of PSR J0740+6620 Using Updated NICER Data, *Astrophys. J.*, 974, 295, doi: [10.3847/1538-4357/ad5fle](https://doi.org/10.3847/1538-4357/ad5fle)
- Drischler, C., Furnstahl, R. J., Melendez, J. A., & Phillips, D. R. 2020a, How Well Do We Know the Neutron-Matter Equation of State at the Densities Inside Neutron Stars? A Bayesian Approach with Correlated Uncertainties, *Phys. Rev. Lett.*, 125, 202702, doi: [10.1103/PhysRevLett.125.202702](https://doi.org/10.1103/PhysRevLett.125.202702)
- Drischler, C., Hebeler, K., & Schwenk, A. 2019, Chiral interactions up to next-to-next-to-next-to-leading order and nuclear saturation, *Phys. Rev. Lett.*, 122, 042501, doi: [10.1103/PhysRevLett.122.042501](https://doi.org/10.1103/PhysRevLett.122.042501)
- Drischler, C., McElvain, K. S., & Arthuis, P. 2026, Many-body perturbation theory for the nuclear equation of state up to fifth order, <https://arxiv.org/abs/2603.24532>
- Drischler, C., Melendez, J. A., Furnstahl, R. J., & Phillips, D. R. 2020b, Quantifying uncertainties and correlations in the nuclear-matter equation of state, *Phys. Rev. C*, 102, 054315, doi: [10.1103/PhysRevC.102.054315](https://doi.org/10.1103/PhysRevC.102.054315)
- Entem, D. R., Machleidt, R., & Nosyk, Y. 2017, High-quality two-nucleon potentials up to fifth order of the chiral expansion, *Phys. Rev. C*, 96, 024004, doi: [10.1103/PhysRevC.96.024004](https://doi.org/10.1103/PhysRevC.96.024004)
- Epelbaum, E., Krebs, H., & Meißner, U. G. 2015, Improved chiral nucleon-nucleon potential up to next-to-next-to-next-to-leading order, *Eur. Phys. J. A*, 51, 53, doi: [10.1140/epja/i2015-15053-8](https://doi.org/10.1140/epja/i2015-15053-8)
- Essick, R., Tews, I., Landry, P., Reddy, S., & Holz, D. E. 2020, Direct Astrophysical Tests of Chiral Effective Field Theory at Supranuclear Densities, *Phys. Rev. C*, 102, 055803, doi: [10.1103/PhysRevC.102.055803](https://doi.org/10.1103/PhysRevC.102.055803)
- Essick, R., Tews, I., Landry, P., & Schwenk, A. 2021, Astrophysical Constraints on the Symmetry Energy and the Neutron Skin of  $^{208}\text{Pb}$  with Minimal Modeling Assumptions, *Phys. Rev. Lett.*, 127, 192701, doi: [10.1103/PhysRevLett.127.192701](https://doi.org/10.1103/PhysRevLett.127.192701)
- Fearick, R. W., von Neumann-Cosel, P., Bacca, S., et al. 2023, Electric dipole polarizability of  $^{40}\text{Ca}$ , *Phys. Rev. Res.*, 5, L022044, doi: [10.1103/PhysRevResearch.5.L022044](https://doi.org/10.1103/PhysRevResearch.5.L022044)
- Feroz, F., Hobson, M. P., & Bridges, M. 2009, MULTINEST: an efficient and robust Bayesian inference tool for cosmology and particle physics, *Mon. Not. Roy. Astron. Soc.*, 398, 1601, doi: [10.1111/j.1365-2966.2009.14548.x](https://doi.org/10.1111/j.1365-2966.2009.14548.x)
- Fonseca, E., Pennucci, T. T., Ellis, J. A., et al. 2016, The NANOGrav Nine-year Data Set: Mass and Geometric Measurements of Binary Millisecond Pulsars, *Astrophys. J.*, 832, 167, doi: [10.3847/0004-637X/832/2/167](https://doi.org/10.3847/0004-637X/832/2/167)
- Fonseca, E., Cromartie, H. T., Pennucci, T. T., et al. 2021, Refined Mass and Geometric Measurements of the High-mass PSR J0740+6620, *Astrophys. J. Lett.*, 915, L12, doi: [10.3847/2041-8213/ac03b8](https://doi.org/10.3847/2041-8213/ac03b8)
- Fraga, E. S., Kurkela, A., & Vuorinen, A. 2014, Interacting quark matter equation of state for compact stars, *Astrophys. J. Lett.*, 781, L25, doi: [10.1088/2041-8205/781/2/L25](https://doi.org/10.1088/2041-8205/781/2/L25)
- Gorda, T., Hebeler, K., Kurkela, A., Schwenk, A., & Vuorinen, A. 2023a, Constraints on Strong Phase Transitions in Neutron Stars, *Astrophys. J.*, 955, 100, doi: [10.3847/1538-4357/aceefb](https://doi.org/10.3847/1538-4357/aceefb)
- Gorda, T., Komoltsev, O., & Kurkela, A. 2023b, Ab-initio QCD Calculations Impact the Inference of the Neutron-star-matter Equation of State, *Astrophys. J.*, 950, 107, doi: [10.3847/1538-4357/acce3a](https://doi.org/10.3847/1538-4357/acce3a)
- Gorda, T., Komoltsev, O., Kurkela, A., & Sunde, E. 2026, Constrained Gaussian-process-bridge Prior for Neutron-star Equation-of-state Inference, *Astrophys. J.*, 1002, 40, doi: [10.3847/1538-4357/ae552a](https://doi.org/10.3847/1538-4357/ae552a)

- Gorda, T., Kurkela, A., Paatelainen, R., Säppi, S., & Vuorinen, A. 2021a, Soft Interactions in Cold Quark Matter, *Phys. Rev. Lett.*, 127, doi: [10.1103/physrevlett.127.162003](https://doi.org/10.1103/physrevlett.127.162003)
- Gorda, T., Kurkela, A., Paatelainen, R., Säppi, S., & Vuorinen, A. 2021b, Cold quark matter at  $N^3\text{LO}$ : Soft contributions, *Phys. Rev. D*, 104, doi: [10.1103/physrevd.104.074015](https://doi.org/10.1103/physrevd.104.074015)
- Göttling, H., Hoff, L., Hebeler, K., & Schwenk, A. 2025, Neutron star crust and outer core equation of state from chiral effective field theory with quantified uncertainties, <https://arxiv.org/abs/2512.19593>
- Greif, S. K., Raaijmakers, G., Hebeler, K., Schwenk, A., & Watts, A. L. 2019, Equation of state sensitivities when inferring neutron star and dense matter properties, *Mon. Not. Roy. Astron. Soc.*, 485, 5363, doi: [10.1093/mnras/stz654](https://doi.org/10.1093/mnras/stz654)
- Hebeler, K., Lattimer, J. M., Pethick, C. J., & Schwenk, A. 2013, Equation of state and neutron star properties constrained by nuclear physics and observation, *Astrophys. J.*, 773, 11, doi: [10.1088/0004-637X/773/1/11](https://doi.org/10.1088/0004-637X/773/1/11)
- Hoogkamer, M., Kini, Y., Salmi, T., Watts, A. L., & Buchner, J. 2025, Cross-Comparison of Sampling Algorithms for Pulse Profile Modeling of PSR J0740+6620, <https://arxiv.org/abs/2502.13682>
- Hoogkamer, M., Rutherford, N., Huppenkothen, D., et al. 2026, Equation-of-state-informed pulse profile modeling, *Phys. Rev. D*, 113, 063049, doi: [10.1103/z2hd-w9sy](https://doi.org/10.1103/z2hd-w9sy)
- Hu, B., Jiang, W., Miyagi, T., et al. 2022, Ab initio predictions link the neutron skin of  $^{208}\text{Pb}$  to nuclear forces, *Nature Phys.*, 18, 1196, doi: [10.1038/s41567-022-01715-8](https://doi.org/10.1038/s41567-022-01715-8)
- Keller, J., Hebeler, K., & Schwenk, A. 2023, Nuclear Equation of State for Arbitrary Proton Fraction and Temperature Based on Chiral Effective Field Theory and a Gaussian Process Emulator, *Phys. Rev. Lett.*, 130, 072701, doi: [10.1103/PhysRevLett.130.072701](https://doi.org/10.1103/PhysRevLett.130.072701)
- Kini, Y., Mauviard, L., Salmi, T., et al. 2026, A NICER View of PSR J0030+0451: Updated Constraints from Six Years of NICER Observations, <https://arxiv.org/abs/2602.23743>
- Koehn, H., Rose, H., Pang, P. T. H., et al. 2025, From Existing and New Nuclear and Astrophysical Constraints to Stringent Limits on the Equation of State of Neutron-Rich Dense Matter, *Phys. Rev. X*, 15, 021014, doi: [10.1103/PhysRevX.15.021014](https://doi.org/10.1103/PhysRevX.15.021014)
- Komoltsev, O., & Kurkela, A. 2022, How Perturbative QCD Constrains the Equation of State at Neutron-Star Densities, *Phys. Rev. Lett.*, 128, doi: [10.1103/physrevlett.128.202701](https://doi.org/10.1103/physrevlett.128.202701)
- Komoltsev, O., Somasundaram, R., Gorda, T., et al. 2024, Equation of state at neutron-star densities and beyond from perturbative QCD, *Phys. Rev. D*, 109, 094030, doi: [10.1103/PhysRevD.109.094030](https://doi.org/10.1103/PhysRevD.109.094030)
- Landry, P., Essick, R., & Chatziioannou, K. 2020, Nonparametric constraints on neutron star matter with existing and upcoming gravitational wave and pulsar observations, *Phys. Rev. D*, 101, 123007, doi: [10.1103/PhysRevD.101.123007](https://doi.org/10.1103/PhysRevD.101.123007)
- Lattimer, J. M. 2021, Neutron Stars and the Nuclear Matter Equation of State, *Annu. Rev. Nucl. Part. Sci.*, 71, 433, doi: [10.1146/annurev-nucl-102419-124827](https://doi.org/10.1146/annurev-nucl-102419-124827)
- Lattimer, J. M. 2023, Constraints on Nuclear Symmetry Energy Parameters, *Particles*, 6, 30, doi: [10.3390/particles6010003](https://doi.org/10.3390/particles6010003)
- Li, A., Watts, A. L., Zhang, G., et al. 2025, Dense matter in neutron stars with eXTP, *Sci. China Phys. Mech. Astron.*, 68, 119503, doi: [10.1007/s11433-025-2761-4](https://doi.org/10.1007/s11433-025-2761-4)
- Lynn, J. E., Tews, I., Carlson, J., et al. 2016, Chiral Three-Nucleon Interactions in Light Nuclei, Neutron- $\alpha$  Scattering, and Neutron Matter, *Phys. Rev. Lett.*, 116, 062501, doi: [10.1103/PhysRevLett.116.062501](https://doi.org/10.1103/PhysRevLett.116.062501)
- Mauviard, L., Guillot, S., Salmi, T., et al. 2025, A NICER View of the 1.4  $M_{\odot}$  Edge-on Pulsar PSR J0614-3329, *Astrophys. J.*, 995, 60, doi: [10.3847/1538-4357/ae145d](https://doi.org/10.3847/1538-4357/ae145d)
- Miller, M. C., Lamb, F. K., Dittmann, A. J., et al. 2019, PSR J0030+0451 Mass and Radius from NICER Data and Implications for the Properties of Neutron Star Matter, *Astrophys. J. Lett.*, 887, L24, doi: [10.3847/2041-8213/ab50c5](https://doi.org/10.3847/2041-8213/ab50c5)
- Miller, M. C., Lamb, F. K., Dittmann, A. J., et al. 2021, The Radius of PSR J0740+6620 from NICER and XMM-Newton Data, *Astrophys. J. Lett.*, 918, L28, doi: [10.3847/2041-8213/ac089b](https://doi.org/10.3847/2041-8213/ac089b)
- Miller, M. C., Dittmann, A. J., Holt, I. M., et al. 2026, The Radius of PSR J0437-4715 from NICER Data, *Astrophys. J. Lett.*, 1000, L48, doi: [10.3847/2041-8213/ae5057](https://doi.org/10.3847/2041-8213/ae5057)
- Ng, S., Legred, I., Suleiman, L., et al. 2025, Inferring the neutron star equation of state with nuclear-physics informed semiparametric models, *Class. Quant. Grav.*, 42, 205008, doi: [10.1088/1361-6382/ae1094](https://doi.org/10.1088/1361-6382/ae1094)
- Punturo, M., Abernathy, M., Acernese, F., et al. 2010, The Einstein Telescope: a third-generation gravitational wave observatory, *Class. Quant. Grav.*, 27, 194002, doi: [10.1088/0264-9381/27/19/194002](https://doi.org/10.1088/0264-9381/27/19/194002)
- Qi, L., Zheng, S., Zhang, J., et al. 2025, PSR J1231-1411 Revisited: Pulse Profile Analysis of X-Ray Observation, *Astrophys. J.*, 981, 99, doi: [10.3847/1538-4357/adb42f](https://doi.org/10.3847/1538-4357/adb42f)

- Raaijmakers, G., Rutherford, N., Timmerman, P., et al. 2025, NEST: A Python package for nested sampling of the neutron star equation of state, *J. Open Source Softw.*, 10, 6003, doi: [10.21105/joss.06003](https://doi.org/10.21105/joss.06003)
- Raaijmakers, G., Riley, T. E., Watts, A. L., et al. 2019, A Nicer View of PSR J0030+0451: Implications for the Dense Matter Equation of State, *Astrophys. J. Lett.*, 887, L22, doi: [10.3847/2041-8213/ab451a](https://doi.org/10.3847/2041-8213/ab451a)
- Raaijmakers, G., Greif, S. K., Riley, T. E., et al. 2020, Constraining the Dense Matter Equation of State with Joint Analysis of NICER and LIGO/Virgo Measurements, *Astrophys. J. Lett.*, 893, L21, doi: [10.3847/2041-8213/ab822f](https://doi.org/10.3847/2041-8213/ab822f)
- Raaijmakers, G., Greif, S. K., Hebeler, K., et al. 2021, Constraints on the Dense Matter Equation of State and Neutron Star Properties from NICER's Mass-Radius Estimate of PSR J0740+6620 and Multimessenger Observations, *Astrophys. J. Lett.*, 918, L29, doi: [10.3847/2041-8213/ac089a](https://doi.org/10.3847/2041-8213/ac089a)
- Read, J. S., Lackey, B. D., Owen, B. J., & Friedman, J. L. 2009, Constraints on a phenomenologically parametrized neutron-star equation of state, *Phys. Rev. D*, 79, doi: [10.1103/physrevd.79.124032](https://doi.org/10.1103/physrevd.79.124032)
- Reed, B. T., Fattoyev, F. J., Horowitz, C. J., & Piekarewicz, J. 2021, Implications of PREX-2 on the Equation of State of Neutron-Rich Matter, *Phys. Rev. Lett.*, 126, 172503, doi: [10.1103/PhysRevLett.126.172503](https://doi.org/10.1103/PhysRevLett.126.172503)
- Reitze, D., Adhikari, R. X., Ballmer, S., et al. 2019, Cosmic Explorer: The U.S. Contribution to Gravitational-Wave Astronomy beyond LIGO, in *Bull. Am. Astron. Soc.*, Vol. 51, 35, doi: [10.48550/arXiv.1907.04833](https://doi.org/10.48550/arXiv.1907.04833)
- Riley, T. E., Watts, A. L., Bogdanov, S., et al. 2019, A NICER View of PSR J0030+0451: Millisecond Pulsar Parameter Estimation, *Astrophys. J. Lett.*, 887, L21, doi: [10.3847/2041-8213/ab481c](https://doi.org/10.3847/2041-8213/ab481c)
- Riley, T. E., Watts, A. L., Ray, P. S., et al. 2021, A NICER View of the Massive Pulsar PSR J0740+6620 Informed by Radio Timing and XMM-Newton Spectroscopy, *Astrophys. J. Lett.*, 918, L27, doi: [10.3847/2041-8213/ac0a81](https://doi.org/10.3847/2041-8213/ac0a81)
- Rutherford, N., Mendes, M., Svensson, I., et al. 2024, Constraining the Dense Matter Equation of State with New NICER Mass-Radius Measurements and New Chiral Effective Field Theory Inputs, *Astrophys. J. Lett.*, 971, L19, doi: [10.3847/2041-8213/ad5f02](https://doi.org/10.3847/2041-8213/ad5f02)
- Salmi, T., Vinciguerra, S., Choudhury, D., et al. 2022, The Radius of PSR J0740+6620 from NICER with NICER Background Estimates, *Astrophys. J.*, 941, 150, doi: [10.3847/1538-4357/ac983d](https://doi.org/10.3847/1538-4357/ac983d)
- Salmi, T., Vinciguerra, S., Choudhury, D., et al. 2023, Atmospheric Effects on Neutron Star Parameter Constraints with NICER, *Astrophys. J.*, 956, 138, doi: [10.3847/1538-4357/acf49d](https://doi.org/10.3847/1538-4357/acf49d)
- Salmi, T., Choudhury, D., Kini, Y., et al. 2024a, The Radius of the High-mass Pulsar PSR J0740+6620 with 3.6 yr of NICER Data, *Astrophys. J.*, 974, 294, doi: [10.3847/1538-4357/ad5f1f](https://doi.org/10.3847/1538-4357/ad5f1f)
- Salmi, T., Deneva, J. S., Ray, P. S., et al. 2024b, A NICER View of PSR J1231-1411: A Complex Case, *Astrophys. J.*, 976, 58, doi: [10.3847/1538-4357/ad81d2](https://doi.org/10.3847/1538-4357/ad81d2)
- Skilling, J. 2004, Nested Sampling, *AIP Conf. Proc.*, 735, 395, doi: [10.1063/1.1835238](https://doi.org/10.1063/1.1835238)
- Somasundaram, R., Svensson, I., De, S., et al. 2025, Inferring three-nucleon couplings from multi-messenger neutron-star observations, *Nature Commun.*, 16, 9819, doi: [10.1038/s41467-025-64756-6](https://doi.org/10.1038/s41467-025-64756-6)
- Svensson, I., Tichai, A., Hebeler, K., & Schwenk, A. 2026, Bayesian approach for many-body uncertainties in nuclear structure: Many-body perturbation theory for finite nuclei, *Phys. Rev. C*, 113, 024303, doi: [10.1103/y8kt-mgf5](https://doi.org/10.1103/y8kt-mgf5)
- Tews, I., Carlson, J., Gandolfi, S., & Reddy, S. 2018, Constraining the speed of sound inside neutron stars with chiral effective field theory interactions and observations, *Astrophys. J.*, 860, 149, doi: [10.3847/1538-4357/aac267](https://doi.org/10.3847/1538-4357/aac267)
- Tews, I., Krüger, T., Hebeler, K., & Schwenk, A. 2013, Neutron matter at next-to-next-to-next-to-leading order in chiral effective field theory, *Phys. Rev. Lett.*, 110, 032504, doi: [10.1103/PhysRevLett.110.032504](https://doi.org/10.1103/PhysRevLett.110.032504)
- Tews, I., Somasundaram, R., Lonardonì, D., et al. 2025, Neutron matter from local chiral effective field theory interactions at large cutoffs, *Phys. Rev. Res.*, 7, 033024, doi: [10.1103/r314-6r62](https://doi.org/10.1103/r314-6r62)
- Vinciguerra, S., Salmi, T., Watts, A. L., et al. 2024, An Updated Mass-Radius Analysis of the 2017-2018 NICER Data Set of PSR J0030+0451, *Astrophys. J.*, 961, 62, doi: [10.3847/1538-4357/acfb83](https://doi.org/10.3847/1538-4357/acfb83)